



Effects of oxide supports on the CO₂ reforming of ethane over Pt-Ni bimetallic catalysts

Zhenhua Xie^{a,b,c}, Binhang Yan^d, Ji Hoon Lee^{b,c}, Qiyuan Wu^e, Xing Li^f, Baohuai Zhao^g, Dong Su^f, Li Zhang^{a,*}, Jingguang G. Chen^{b,c,**}



^a College of Power Engineering, Chongqing University, Chongqing 400044, China

^b Department of Chemical Engineering, Columbia University, New York, NY 10027, United States

^c Chemistry Division, Brookhaven National Laboratory, Upton, NY 11973, United States

^d Department of Chemical Engineering, Tsinghua University, Beijing 100084, China

^e Material Science and Chemical Engineering, Stony Brook University, Stony Brook, NY 11794, United States

^f Center for Functional Nanomaterials, Brookhaven National Laboratory, Upton, NY 11973, United States

^g School of Materials Science and Engineering, Tsinghua University, Beijing 100084, China

ARTICLE INFO

Keywords:
CO₂ reforming
Ethane
Pt
Ni
Support effect

ABSTRACT

Catalytic reduction of CO₂ by ethane creates an opportunity to use the shale gas and CO₂ as the raw materials to produce syngas *via* dry reforming. In the present work, Pt-Ni bimetallic catalysts were investigated on reducible (CeO₂, TiO₂) and irreducible (γ -Al₂O₃, SiO₂) oxides. The results showed that catalysts supported on reducible oxides, especially CeO₂, were more active than those supported on irreducible oxides. Pulse and flow reactor studies and infrared spectroscopy experiments revealed a bi-functional Mars-Van Krevelen redox mechanism on PtNi/CeO₂ and a mono-functional Langmuir-Hinshelwood mechanism on PtNi/SiO₂, providing insights into the effects of reducibility of oxide supports on the reaction kinetics. Additionally, compared with the non-reducible SiO₂, *in situ* X-ray diffraction (XRD) and pulse reactor analysis revealed that CO₂ could be effectively activated on the reducible CeO₂ and formed surface oxygen species to promote ethane dissociation into active carbon species. Thermogravimetric analysis (TGA), Transmission electron microscopy (TEM) and Raman spectroscopy showed that cokes formed on PtNi/CeO₂ were primarily disordered/amorphous carbon species that could be easily removed during reforming.

1. Introduction

The emission of CO₂, mainly from the consumption of fossil fuels, is considered as a major cause of climate change and ocean acidification [1–3]. Thus the mitigation and utilization of CO₂ are critical. The huge shale gas reserve provides an opportunity to use light alkanes to activate CO₂. Ethane is the second largest component (*ca.* 10%) of shale gas after methane [4]. The activation of CO₂ by ethane can occur *via* two distinct pathways: 1) dry reforming of ethane (DRE) with C–C bond rupture to produce syngas (C₂H₆ + 2CO₂ → 4CO + 3H₂) and 2) oxidative dehydrogenation of ethane with CO₂ (ODEC) with C–H bond scission to form ethylene (C₂H₆ + CO₂ → C₂H₄ + CO + H₂O) [5]. Based on thermodynamic calculations DRE becomes spontaneous at a temperature that is ~100 K lower than that for dry reforming of methane (DRM), making it feasible for the process to be operated under milder

conditions and help reduce catalyst deactivation [6].

For reforming reactions, Ni-based catalysts are widely used in the industry for syngas production due to their relatively high activity, although significant catalyst deactivation, mainly by coke deposition, usually occurs during the dry reforming process [7]. In contrast, precious metal-based catalysts (Pt, Pd, Rh, Ru, Ir) typically show higher activity and stability, but it is less economical for large-scale processes due to their limited availability and high cost [8]. However, doping precious metal [9] on Ni-based catalysts should provide an alternative choice since bimetallic catalysts usually outperform their parent metals with unique properties. Miguel et al. [10] and García-Díéguez et al. [11,12] reported that Pt-Ni bimetallic clusters promoted the reducibility of Ni and inhibited carbon deposition, leading to a higher activity and stability for DRM than either monometallic catalyst. Moreover, Kattel et al. performed density functional theory (DFT)

* Corresponding author.

** Corresponding author at: Department of Chemical Engineering, Columbia University, New York, NY, 10027, United States.

E-mail addresses: lizhang@cqu.edu.cn (L. Zhang), jgchen@columbia.edu (J.G. Chen).

calculations of DRE and revealed that the PtNi(111) surface should be highly selective to the oxidative C–C bond cleavage of ethane to syngas [13].

In addition to the active metal components, oxide supports also play a significant role in improving the catalytic activity and resistance to coke deposition. Various supports with different reducibility have been widely investigated, including reducible (CeO_2 and TiO_2) and irreducible (SiO_2 and Al_2O_3) oxides. Reducible oxides are generally characterized by their possible strong metal-support interaction (SMSI) and redox behavior [8]. The SMSI effect usually appears at high reduction temperatures ($> 773 \text{ K}$). It may reduce the catalytic activity via the blockage of active site, while it can also help enhance the catalytic activity and inhibit coke deposition by the electronic metal-support interactions and the decoration of metal by the reduced oxide support [14–20]. Tóth et al. examined various Au-based catalysts and found that ethane conversion was noticeably enhanced on TiO_2 , CeO_2 and ZnO compared to the insulating materials, MgO and Al_2O_3 [21]. They attributed this difference mainly to the electronic interaction that promoted the formation of negatively charged CO_2 . Similar conclusions were drawn for the reaction of propane with CO_2 [22]. On the other hand, the surface lattice defects of reducible oxide supports can also impart a redox behavior to help CO_2 activation and carbon gasification [23,24]. Among them, CeO_2 with its high oxygen storage/release capacity is widely used as a promoter or support to enhance CO_2 activation and subsequently establish an oxygen pool that suppresses coke deposition by means of the redox behavior of $\text{Ce}^{3+}/\text{Ce}^{4+}$ [25–27]. The CO_2 -support interaction also becomes significant in the case of reducible supports with a bi-functional mechanism [8]. Wang et al. reported that methane was activated on metal sites, while CO_2 activation was mainly promoted by the reduced CeO_x or the metal-support boundary [26]. In contrast, on irreducible substrates, such as SiO_2 supported catalysts, the activation of both alkane and CO_2 appeared to occur on the metal sites, leading to a mono-functional mechanism that did not involve the participation of the oxide support [28].

At present, much attention has been focused on the dehydrogenation [6,29–31] and aromatization of ethane [32]. In contrast, only limited attention has been focused on the dry reforming of ethane; its kinetics and mechanism, if any, were merely on the steam reforming of ethane (SRE) [33,34]. To our knowledge, Kattel et al. established the first complex reaction network of DRE on PtNi(111) by the combined approaches of DFT calculations and Monte Carlo simulations. The formation of ${}^*\text{C}_2\text{H}_y\text{O}$ intermediates from ${}^*\text{C}_2\text{H}_y$ and ${}^*\text{O}$ was proposed to be essential for the oxidative C–C bond cleavage to form CO [13]. In addition, Tóth et al. found that Au/TiO₂ was an ODEC catalyst, while Au/CeO₂ and Au/ZnO catalysts were favorable for DRE, indicating that reaction pathways could be tuned by using different oxide supports [21].

In the present work, we investigated the effects of supports including the reducible (*i.e.*, CeO_2 and TiO_2) and irreducible (*i.e.*, SiO_2 and $\gamma\text{-Al}_2\text{O}_3$) oxides on the Pt-Ni bimetallic catalysts for CO_2 reduction by ethane. The results showed that PtNi/CeO₂ was the best candidate among the four catalysts for DRE with the highest activity and CO yield. Thus, it was chosen as a representative of reducible catalyst for additional kinetics studies at different temperatures and reactant partial pressures. PtNi/SiO₂ was also investigated as a reference of irreducible oxide to highlight the support effect on the kinetics of the DRE reaction.

2. Experimental

2.1. Catalyst preparation

Four oxide supports were used to synthesize the Pt-Ni bimetallic catalysts with incipient wetness impregnation (IWI) or slurry phase impregnation (SPI) methods. For the high surface area supports, $\gamma\text{-Al}_2\text{O}_3$ (80–120 m²/g, Alfa Aesar), TiO_2 (240 m²/g, amorphous anatase, Alfa Aesar) and SiO_2 (168 m²/g, Alfa Aesar), the IWI method was

employed, while for the low surface area support, CeO_2 (35–45 m²/g, cubic, Sigma-Aldrich), the SPI method was used. Both IWI and SPI methods were adapted from Ref. [35]. In order to maximize the extent of Pt-Ni bimetallic bond formation, a co-impregnation procedure was used to achieve the loading amounts of 1.67 wt% Pt ($\text{Pt}(\text{NH}_3)_4(\text{NO}_3)_2$, Alfa Aesar) and 1.51 wt% Ni ($\text{Ni}(\text{NO}_3)_2 \cdot 6\text{H}_2\text{O}$, Alfa Aesar), corresponding to a Pt:Ni atomic ratio of 1:3 [36]. All the catalysts were dried at 373 K for 10 h and then calcined at 563 K for 2 h, with a heating ramp rate of 0.4 K/min and 0.8 K/min, respectively.

2.2. Catalyst characterization

Brunauer-Emmett-Teller (BET) measurements were performed using an AMI-300ip (Altamira) instrument to determine the specific area of catalysts. The sample (~100 mg) was pretreated with helium (He) at 393 K for 30 min to desorb gases such as moisture adsorbed on the catalysts. N₂ adsorption was then carried out at 77 K and continuously recorded with a thermal conductivity detector (TCD).

Pulsing CO chemisorption was measured to determine the number of active sites using the same AMI-300ip (Altamira) instrument. A quartz reactor was loaded with ~200 mg of catalyst, which was then reduced in a mixture of H₂-He (totally 40 ml/min, 1:1 ratio) at 723 K for 1 h and cooled down in He before pulsing 37 ml/min CO in He. The amount of CO flowing out the quartz reactor was monitored by a TCD. The ratio of chemisorbed CO and active site was assumed to be 1:1, allowing qualitative comparison of the number of active sites among different supported catalysts.

In situ X-ray diffraction (XRD) measurements of different catalysts were carried out within a compact flow cell at 17 BM-B ($\lambda = 0.24141 \text{ \AA}$) of the Advanced Photon Source (APS) at Argonne National Laboratory. Details of the compact flow cell setup have been previously provided [37–39]. Catalyst was reduced *in situ* by a mixture of H₂/He (5/5 ml/min) with the temperature ramping from room temperature to 723 K (10 K/min) and holding for 30 min. Afterwards, temperature was increased to 873 K (10 K/min) and then the catalyst was sequentially exposed to the reaction gases ($\text{CO}_2/\text{C}_2\text{H}_6/\text{He} = 2.5/2.5/5 \text{ ml/min}$) for 60 min, mixture of CO_2/He (5/5 ml/min) for 30 min and mixture of H₂/He for 30 min (5/5 ml/min). The two-dimensional (2D) diffraction images were continuously collected by a Perkin Elmer Amorphous Silicon detector. The 2D images were subsequently integrated by the program Fit2D [40] to obtain XRD profiles. Structural refinement was performed with the GSAS Rietveld software [41,42].

Diffuse Reflectance Infrared Fourier Transform Spectroscopy (DRIFTS) experiments were carried out with an FTIR spectrometer (Thermo Nicolet 6700) to investigate the CO adsorption on the bimetallic and monometallic catalysts and CO_2 adsorption on the bimetallic catalysts. Each sample was reduced under a H₂/He mixture (1:3) at 723 K, prior to the background spectrum collection at room temperature. For CO adsorption experiments, the sample was then exposed to a CO/He mixture (1:3) for 30 min. After a pure He purging (30 min), the sample spectrum was collected (512 scans) at a resolution of 4 cm^{−1}. For CO_2 adsorption experiments, the pre-reduced sample was heated to 773 K under He atmosphere before a background spectrum collection. Then, a mixture of CO_2/He (5/15 ml/min, 30 min) or $\text{CO}_2/\text{H}_2/\text{He}$ (5/5/10 ml/min, 30 min) was purged into the reaction cell. All DRIFTS spectra (Kubelka – Munk unit) for CO_2 adsorption were continuously collected with 64 scans at a resolution of 4 cm^{−1}.

Temperature programming oxidation-thermogravimetric analysis (TPO-TGA) was used to determine the amount of coke deposited on the spent catalysts. About 30 mg of spent sample was loaded and dried by Ar (30 ml/min) at 473 K for 30 min, followed by cooling down to room temperature. The sample was weighed again and then heated with a ramping rate of 10 K/min from room temperature to 1273 K in Air (100 ml/min). The relative mass losses in the TPO-TGA profiles allowed a quantitative comparison for the amounts of coke deposited on different spent catalysts. The position and area of the derivative

thermogravimetric (DTG) peaks were used to correlate with the type and amount of carbonaceous species, respectively.

Raman spectroscopy was used to characterize the structure of the coke deposited on the spent catalysts using a Renishaw inVia Confocal Raman microscope with a 50× objective lens. The spent samples were excited by a 532 nm laser at the range of 1000–2000 cm⁻¹. Spectra were collected by four scans with an exposure time of 10 s.

The distribution of metal particles and morphologies of carbon species on the four Pt-Ni catalysts were characterized using a transmission electron microscopy (TEM; JEM-2100, 200 kV). Scanning Transmission Electron Microscopy (STEM)-Energy Dispersive Spectroscopy (EDS) mapping was performed within an FEI Talos F200X TEM (operated at 200 keV) equipped with an energy dispersive X-ray spectrometer. Reduced or spent catalysts were ultrasonically dispersed in ethanol for 10 min. Afterwards, a droplet was dripped onto a lacey copper grid and fully dried before use.

2.3. Catalytic performance evaluations

2.3.1. Flow reactor studies

Catalytic performance was evaluated in a flow packed-bed quartz tubular reactor (1/4 inch O.D.) under atmospheric pressure, utilizing 100 mg catalyst (40–60 mesh) loaded between two quartz wool plugs at the center of the reactor. The experimental set-up was shown in Fig. S1 of Supporting Information (SI). Temperature profile within the reactor was tested and the isothermal condition was ensured with the temperature difference between the inlet and outlet of the catalytic bed being < 3 K. Prior to each experiment, the catalyst was pretreated *in situ* at 723 K for 1 h with a mixture of H₂ and Ar (total flow rate of 40 ml/min, 1:1 feed ratio), and then cooled down to room temperature in the Ar flow (20 ml/min). Reactants (C₂H₆, CO₂) diluted with Ar were subsequently fed into the reactor via mass flow controllers (Brooks 5850E) with a flow ratio of 1:1:2 at a total flow rate of 40 ml/min. The catalyst bed was heated to 873 K at a ramp rate of 10 K/min and then held in the stream for 12 h to achieve a pseudo-steady state. The outlet stream was analyzed online using a gas chromatography (Agilent 7890B) equipped with a TCD and flame ionization detector (FID). Water within the outlet stream was removed by a condenser. Ar was used as an internal standard to account for the volume effects due to the high temperature during the reaction. The analysis procedures led to a 100 ± 2% closure of carbon balance. Control experiments without using catalysts were performed to evaluate possible contributions from the gas-phase reaction and quartz wall to the overall reaction, showing a negligible ethane conversion of less than 0.1%. In the reactions with pure oxide supports, the activity was also negligible under experimental conditions used in the current study. The conversion (X) and turnover frequency (TOF) of species *i* were calculated via Eqs. (1) and (2), respectively:

$$X_i = \frac{[F_i]_{in} - [F_i]_{out}}{[F_i]_{in}} \times 100\% \quad (1)$$

$$TOF_i = \left| \frac{[F_i]_{in} - [F_i]_{out}}{CO \text{ uptake} \cdot m_{catalyst}} \right| \quad (2)$$

where [F_i]_{in} and [F_i]_{out} referred to the inlet and outlet molar flow rate, respectively, of species *i* corrected by the Ar molar flow rate (mol/min); CO uptake (μmol/g) and *m_{catalyst}* (mg) indicated the number of active site per unit mass of catalyst and the mass of catalyst, respectively.

The selectivity (*S*) and yield (*Y*) of carbon-containing species (CO, C₂H₄, CH₄, and C₃+) were defined as Eqs. (3)–(5) based on the consumption of C₂H₆:

$$S_i = \frac{[F_i]_{out}}{[F_{C_2H_6}]_{in} - [F_{C_2H_6}]_{out}} \times \frac{n_{carbon-atoms,i}}{n_{carbon-atoms,C_2H_6}} \times 100\% \quad (3)$$

$$S_{CO} = 1 - \sum_{i \neq CO} S_i \times 100\% \quad (4)$$

$$Y_i = X_i \cdot S_i \quad (5)$$

2.3.2. Pulse reactor studies

The activation capacity of different catalysts for reactants was quantified by pulse reactor experiments. As illustrated in Fig. S2 of SI, the pulse reactor system operates in three optional modes: pretreatment, purging and pulsing. For each experiment, ~20 mg of catalyst was loaded and pretreated by a mixture of H₂/Ar (2/18 ml/min) at 873 K for 2 h, followed by the purging of GC carrier gas (Ar) for 15 min. Then the mixture of reaction gases (CO₂/N₂ or C₂H₆/N₂ = 1:9, N₂—internal standard gas), sampled by a loop (1 ml), was pulsed into the catalyst bed to carry out reaction at 873 K. The exhaust was analyzed and quantified using the same GC setup as the flow reactor system.

2.4. Kinetics measurements

2.4.1. Elimination of mass and heat transport limitations

The reaction rates of C₂H₆ and CO₂ were determined within a differential plug flow tubular reactor under the isothermal and atmospheric pressure condition. The reactor set-up and analytical methods were the same as those used for the catalytic performance test (Section 2.3.1), except that water vapor was retained by heating tapes (> 413 K) and calibrated by the reverse water-gas shift (RWGS) reaction on Pt/CeO₂ at 513–673 K. The elemental (C, H, O) balances were around 100%. Two rules of thumb for the plug flow pattern [43] were fulfilled as follows: *d_r/d_p* > 10 and *L/d_r* > 5, where *L* is the catalyst bed length (~3 cm), *d_r* and *d_p* refer to the diameter of the reactor (~4 mm) and the catalyst particle (0.2–0.4 mm), respectively.

It is critical to measure the correct kinetics data free of transport limitations as required by the benchmarking in catalysis science [44]. In the chemically-controlled regime, catalytic reaction rate should be proportional to the number of active sites per unit volume [45,46]. Therefore, pure catalysts were intra- and inter-diluted using SiO₂ and acid-purified quartz particles, respectively, to reduce the reaction rate per unit volume, thus reducing axial or radial temperature gradients. Conversion of ethane was kept below 8% to reduce the axial reactant concentration gradients to achieve a differential flow reactor configuration. As shown in Fig. 1, net C₂H₆ reaction rate was measured at 873 K as a function of residence time to check the effects of particle size and dilution ratio on the reaction rate. It shows that the measured reaction rate was independent of the particle size and particle dilution ratio, indicating that the reaction was free of heat and mass transport limitations. This was further numerically validated for the highest reaction rate under conditions employed for the kinetics experiments by a series of criteria [47–56] for the absence of temperature and concentration gradients within intra-particle, inter-phase and inter-particle (Section S2 in SI). As one can expect, the resulting activation barriers (shown in Section 3.3.1) were higher than the apparent values in Ref. [39].

2.4.2. Acquisition of forward reaction rates

Fig. 1 shows that the measured/net C₂H₆ reaction rate was almost the same at different residence time, indicating that the reversibility of the overall reaction was negligible, which could be further verified by the approach to equilibrium factors (*η*), i.e., reversibility [57] for the DRE and RWGS reactions:

$$\eta_1 = \frac{[P_{CO}]^4 [P_{H_2}]^3}{[P_{CO_2}]^2 [P_{C_2H_6}]} \times \frac{1}{K_{eq,1}} \quad (6)$$

$$\eta_2 = \frac{[P_{CO}] [P_{H_2O}]}{[P_{CO_2}] [P_{H_2}]} \times \frac{1}{K_{eq,2}} \quad (7)$$

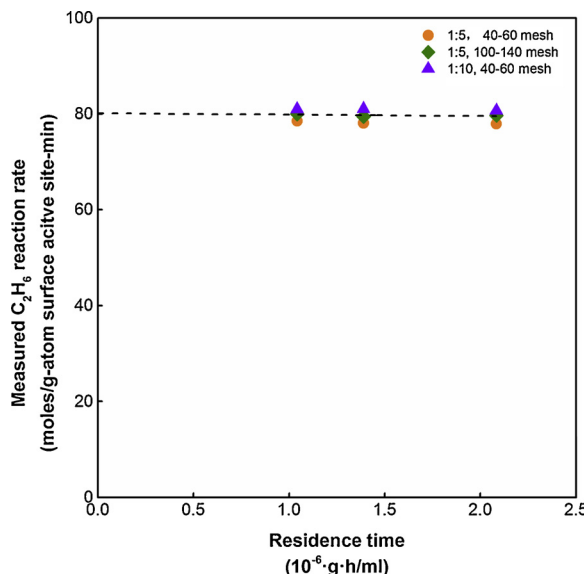


Fig. 1. Trend of the measured C_2H_6 reaction rate along with the residence time on $PtNi/CeO_2$ at 873 K. The trend was demonstrated by the dashed line. Test conditions: $m_{PtNi-CeO_2} = 5 \text{ mg}$, (●) $R_{\text{intra}} = 1:5$, $R_{\text{inter}} = 1:80$, 40–60 mesh; (◆) $R_{\text{intra}} = 1:5$, $R_{\text{inter}} = 1:80$, 100–140 mesh; (▲) $R_{\text{intra}} = 1:10$, $R_{\text{inter}} = 1:80$, 40–60 mesh; R_{intra} and R_{inter} was defined as the mass ratio of $PtNi/CeO_2$ to SiO_2 (intra-particle dilution) and acid-purified quartz (inter-particle dilution), respectively. Residence time was represented by the reciprocal of weight hourly space velocity.

where $[P_i]$ is the average partial pressure (in atm) of species i between the inlet and outlet of the reactor, and $K_{eq,1}$ and $K_{eq,2}$ are the equilibrium constants for the DRE and RWGS reactions, respectively.

η_1 was much smaller than unity with a magnitude of 10^{-15} – 10^{-10} , indicating that the DRE reaction was very far away from equilibrium. Thus the measured/net reaction rate of C_2H_6 can be directly used to represent the forward reaction rate of C_2H_6 with no need to be corrected by η_1 . However, the RWGS reaction had a much higher η_2 , ranging from 0.1 to 0.5. Therefore, η_2 was used to correct the contribution from reverse reaction rate to obtain the forward reaction rate of the RWGS reaction. In the kinetics tests, all the forward reaction rates were obtained as follows:

$$TOF_{C_2H_6,f} = TOF_{C_2H_6,m} = \frac{TOF_{CO,DRE,f}}{4} + TOF_{C_2H_4,f} \quad (8)$$

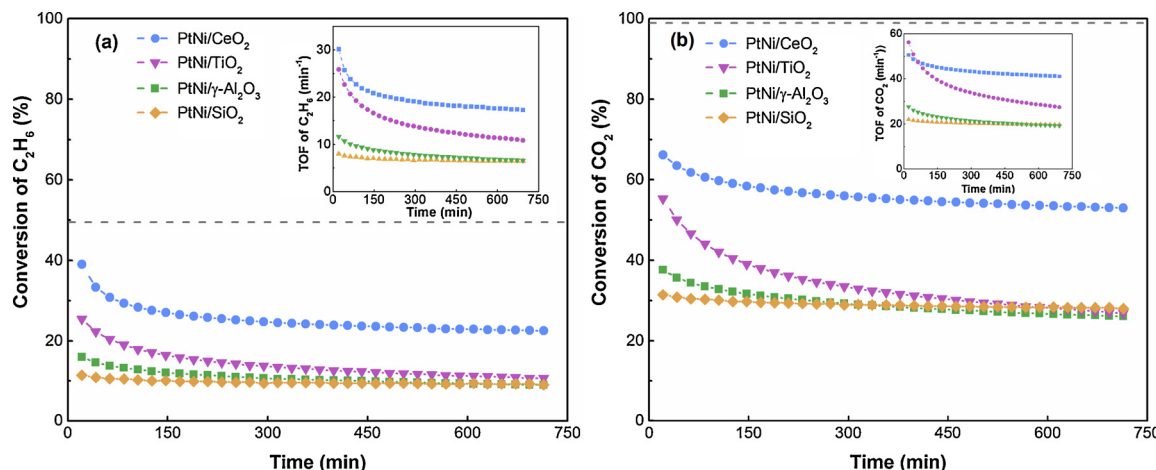


Fig. 2. Conversion of (a) C_2H_6 and (b) CO_2 on different supported Pt-Ni bimetallic catalysts at 873 K. Insets in figures (a) and (b) correspond to the TOF plots of C_2H_6 and CO_2 at 873 K. The gray dashed lines represent the equilibrium conversion of C_2H_6 (49.3%) and CO_2 (98.9%) at 873 K.

$$TOF_{CO_2,f} = \frac{TOF_{CO,DRE,f}}{2} + TOF_{CO,RWGS,f} \quad (9)$$

$$TOF_{CO,DRE,f} = TOF_{CO,m} - TOF_{H_2O,m} \quad (10)$$

$$TOF_{CO,RWGS,f} = \frac{TOF_{H_2O,m}}{1 - \eta_2} \quad (11)$$

$$TOF_{C_2H_4,f} = TOF_{C_2H_4,m} \quad (12)$$

where $TOF_{i,f}$ and $TOF_{i,m}$ are the forward and measured turnover frequency (min^{-1}) of species i , respectively.

Kinetics experiments were carried out within the temperature range of 813–873 K (10 K/step) and partial pressure range of C_2H_6 or CO_2 from 6.25 kPa to 62.5 kPa. To avoid the interference of catalyst deactivation on the activation barriers measurements, the method for deactivating reactions reported in our previous work was adopted here [58]. The reaction rates used for kinetics evaluations referred to the values under the steady state.

3. Results and discussion

3.1. Catalytic performance

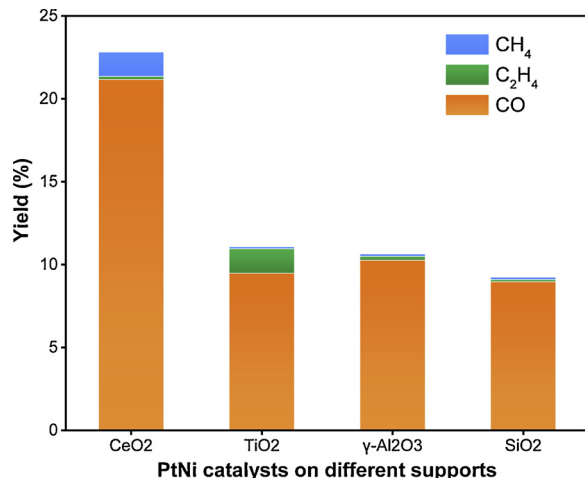
Fig. 2 compares the conversion as well as turnover frequency (TOF) of reactants with time on stream over different catalysts. The results of the initial (the first 21 min) and pseudo-steady (PS) catalytic performance over different Pt-Ni bimetallic catalysts are summarized in Table 1. The initial conversion of CO_2 and C_2H_6 over different supported Pt-Ni catalysts followed the trend of $CeO_2 > TiO_2 > \gamma-Al_2O_3 > SiO_2$, while it changed to $CeO_2 > TiO_2 \approx \gamma-Al_2O_3 \approx SiO_2$ at the PS state. If normalized by CO uptake values, the TOF values at the PS state kept a similar trend except for $PtNi/TiO_2$ due to its low CO uptake value. In general, the reducible supports (CeO_2 and TiO_2) presented a higher activity than those of irreducible ones (SiO_2 and $\gamma-Al_2O_3$). It should be noted that $PtNi/CeO_2$ was the most active catalyst among the four catalysts with the highest conversion of CO_2 (53.4%) and C_2H_6 (22.8%) at the PS state. These values were approximately twice as high as those of the other three catalysts.

As shown in Table 1, CO, C_2H_4 and CH_4 were the main carbon-containing products, representing DRE, dehydrogenation (DE) and cracking of C_2H_6 , respectively. Because of the significant differences in the conversions of C_2H_6 and CO_2 over different supported catalysts, the product yield, instead of selectivity, is used to qualitatively compare the trend in product distribution. Fig. 3 presents the support effects on the C_2H_6 -based yield over different Pt-Ni bimetallic catalysts at the PS state. CO was the dominant product on all the catalysts, indicating that the

Table 1

Summary of specific surface area, CO uptake, and catalytic results over different Pt-Ni bimetallic catalysts at the pseudo-steady state.

Catalysts	S _{BET} (m ² /g)	CO uptake (μmol/g _{cat})	Conversion		TOF (min ⁻¹) ^a		C ₂ H ₆ -based selectivity (%) ^a		
			CO ₂	C ₂ H ₆	CO ₂	C ₂ H ₆	CO	C ₂ H ₄	CH ₄
PtNi/CeO ₂	44.5	51.8	53.4	22.8	42.7	18.2	92.8	0.8	6.5
PtNi/TiO ₂	184.8	40.9	27.9	11.1	28.2	11.2	85.5	13.4	1.1
PtNi/γ-Al ₂ O ₃	83.3	56.3	26.5	9.2	19.4	6.7	93.0	3.4	3.6
PtNi/SiO ₂	160.5	59.0	28.2	9.2	19.8	6.5	97.0	1.5	1.5

^a represents the data averaged between 567 and 693 min.**Fig. 3.** Support effects on the ethane-based yield of Pt-Ni bimetallic catalysts for the catalytic reduction of CO₂ with ethane at 873 K. Pseudo-steady state: 567–693 min.

dominant reaction pathway was DRE via the C–C bond cleavage. It should be noted that PtNi/CeO₂ presented the highest CO yield (~21%), about twice as high as the others.

The comparison of catalytic performance among the different supported Pt-Ni bimetallic catalysts demonstrated that catalysts supported on reducible oxides, especially PtNi/CeO₂, were more active than those supported on irreducible oxides. The remainder of this manuscript was focused on the structural analyses of oxide supports and their effects on the kinetics of catalytic reduction of CO₂ by C₂H₆. PtNi/CeO₂ was chosen as a representative of reducible supports due to its high and stable activity; PtNi/SiO₂ was also examined as a reference of irreducible support.

3.2. Characterization of fresh and spent catalysts

As shown in Table 1, the four catalysts showed quite different specific surface areas with the trend of PtNi/TiO₂ (184.8 m²/g) > PtNi/SiO₂ (160.5 m²/g) > PtNi/Al₂O₃ (83.3 m²/g) > PtNi/CeO₂ (44.5 m²/g), although the catalysts had similar CO uptake values except PtNi/TiO₂. Fig. 4 (a1)-(d1) reveal a similar metal particle size distribution (~2 nm) on the four reduced samples except a slightly larger size (2.85 ± 0.03 nm) on PtNi/Al₂O₃. After reaction, Fig. 4 (a2)-(d2) show that metal particles on the spent PtNi/CeO₂ (2.48 ± 0.04 nm) and PtNi/SiO₂ (2.35 ± 0.04 nm) nearly maintained stable with negligible agglomeration. It should be noted that smaller size of particles (1.73 ± 0.03 nm) was observed on the spent PtNi/TiO₂, whereas the conversions on PtNi/TiO₂ decreased continuously with the time on stream. This was most likely due to the SMSI effect since, in the presence of hydrogen, the reduced TiO_x species could migrate to block some of the metal active sites at high temperatures (> 773 K) [14,15]. The high resolution TEM image (Fig. S4(a) in SI) clearly exhibited an amorphous encapsulation layer on the surface of metal particles.

Although the metal decoration may also take place on CeO₂ supported catalysts, a higher reduction temperature, at least 973 K, is usually needed [15]. In contrast, metal particles significantly aggregated into larger size of 7.50 ± 0.12 nm with Pt-Ni particle disintegration (Fig. S4(d) and (e) in SI) on the spent PtNi/Al₂O₃, consistent with the continuously decreasing trend in the conversions. The comparison of the TEM results suggested that metal particle size was not likely an only key factor for the different catalytic activity on the four catalysts, even though the variation of metal particle size may affect the stability.

Coke deposition is usually considered as one of the main reasons for catalyst deactivation in dry reforming reactions. As shown in Fig. 5 (a), TPO-TGA was used to quantify coke deposition on different supported catalysts. To make a quantitative comparison of the coke amount over different catalysts, the DTG plots were deconvoluted by multiple Gaussian functions, which showed a good fitting to the DTG profiles (Fig. S5(a)-(d) in SI). The peak positions (T_p) and corresponding peak areas (A_p) of DTG plots in Fig. 5 (b) could be correlated with the types and amount of carbon species, respectively. The D band of Raman spectroscopy was associated with the disordered defective carbon structure (e.g., amorphous carbon or defective filament carbon [59]), while the G band reflected the ordered and well-graphitized carbon structures [60]. Thus, the intensity ratio of the G band (I_G) and D band (I_D) was used to qualitatively compare the fractions of ordered and disordered carbons on different catalysts [61]. For ease of comparison, the Raman spectra were normalized to have the same intensity of the D band.

As shown in Fig. 5 (a) and Table 2, the coke amount from TGA results followed the trend of PtNi/CeO₂ (15.5%) > PtNi/SiO₂ (3.6%) ≈ PtNi/γ-Al₂O₃ (3.2%) > PtNi/TiO₂ (1.7%). Flow reactor study and TGA analysis indicated that PtNi/CeO₂ exhibited the highest C₂H₆ conversion (22.8%) with the highest coke deposition. PtNi/TiO₂ showed the lowest amount of coke deposition, which could be attributed to the TiO_x species induced by reduction to geometrically block the highly coordinated active sites necessary for coke deposition [16]. Both PtNi/γ-Al₂O₃ and PtNi/SiO₂ exhibited a similar and relatively low amount of coke deposition. However, the DTG results demonstrated that less percentage of deposited coke existed above 800 K on PtNi/CeO₂ (2.5%) and PtNi/TiO₂ (7.4%) than the counterparts on PtNi/γ-Al₂O₃ (23.9%) and PtNi/SiO₂ (36.8%). It is well known that coke removed at high temperature during TGA experiment usually correlates with stable carbon species like graphitic carbon. This is supported by the Raman results (Fig. 6 (a) and Table 3) that the I_G/I_D ratios of different spent catalysts followed the trend of PtNi/CeO₂ (0.72) < PtNi/TiO₂ (0.75) < PtNi/γ-Al₂O₃ (1.04) < PtNi/SiO₂ (1.24). Moreover, Fig. 6 (b) shows that the sum of DTG peak areas correlated very well with the Raman ratio of I_G/(I_D + I_G), suggesting that the carbon species under the Peak-1/Peak-2 and Peak-3/Peak-4 should be associated with disordered and ordered carbon structures, respectively. Thus, the coke deposited on PtNi/CeO₂ and PtNi/TiO₂ was more disordered, while the counterparts on PtNi/γ-Al₂O₃ and PtNi/SiO₂ were more ordered. This is consistent with the TEM imaging demonstrated in Fig. S4 of SI. For spent PtNi/CeO₂, Fig. S4(b) in SI clearly demonstrates that not only the metal particle but also the support was encapsulated by carbonaceous species,

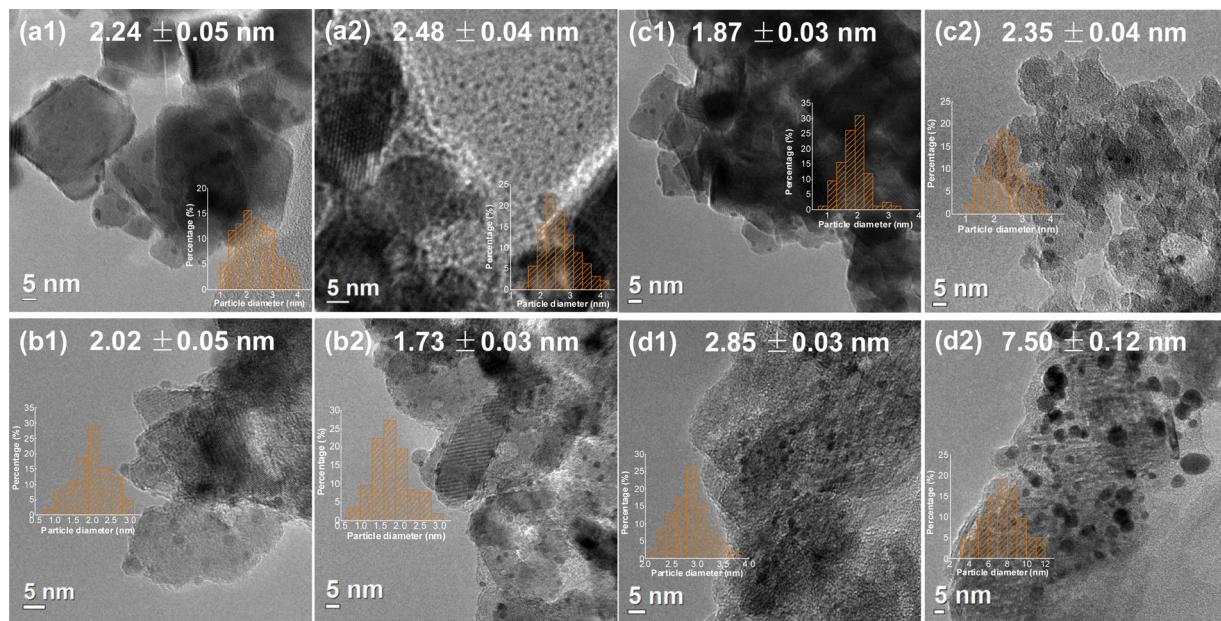


Fig. 4. TEM images of reduced samples: PtNi/CeO₂ (**a1**), PtNi/TiO₂ (**b1**), PtNi/SiO₂ (**c1**) and PtNi/Al₂O₃ (**d1**), and spent samples: PtNi/CeO₂ (**a2**), PtNi/TiO₂ (**b2**), PtNi/SiO₂ (**c2**), and PtNi/Al₂O₃ (**d2**) with the metal particle size distribution.

however, mainly in the amorphous morphology. This indicates that amorphous carbon formed on the CeO₂ supported Pt-Ni catalyst could diffuse from metal sites onto the support. For PtNi/TiO₂, the TEM image also exhibits negligible carbon species (Fig. S4(a) in SI) on the spent sample. For PtNi/γ-Al₂O₃, Fig. S4(c) in SI shows that metal particles were encapsulated by an ordered layer with carbon nano-onion (CNO) like feature, which should contribute to the deactivation. For PtNi/SiO₂, as shown in Fig. S4(f) and (g) in SI, besides the CNO surrounding the metal particles, multi-wall nanotubes were observed as well, consistent with the graphic carbon indicated by the DTG signal and the high ratio of I_G/I_D from Raman study. However, it was resistant to deactivation, most likely benefiting from the strong metal–silica bonding interactions [62] and large surface area which provides more space to accommodate carbonaceous species.

Fig. 7(a) and (b) show the sequential *in situ* XRD spectra of PtNi/

CeO₂ and PtNi/SiO₂ under different treatment conditions. The standard spectra of Pt, PtO, Ni and NiO were shown in Fig. S6 in SI. As shown in Fig. 7(a), peaks associated with NiO [fcc: (111): 5.66°] were barely observed at room temperature, whereas the metallic Ni phase [fcc: (111): 6.80°] appeared from ~470 K during the heating process to 723 K under H₂ atmosphere. Moreover, the broadness of Ni peaks became narrower with increasing temperature until 723 K and maintained nearly unchanged during the subsequent dwelling period at 723 K as well as the heating period under He toward 873 K. This suggested that the NiO species should be highly dispersed on the surface or inside the CeO₂ support of the as-prepared catalyst, and could be crystallized by reduction. After exposing to the reactant stream (CO₂ + C₂H₆), significant changes were observed in the XRD spectra at the initial reaction period (~20 min) that the peaks correlated with Ni phases disappeared while those assigned with NiO peaks [(111): 5.66°, (200): 6.55°]

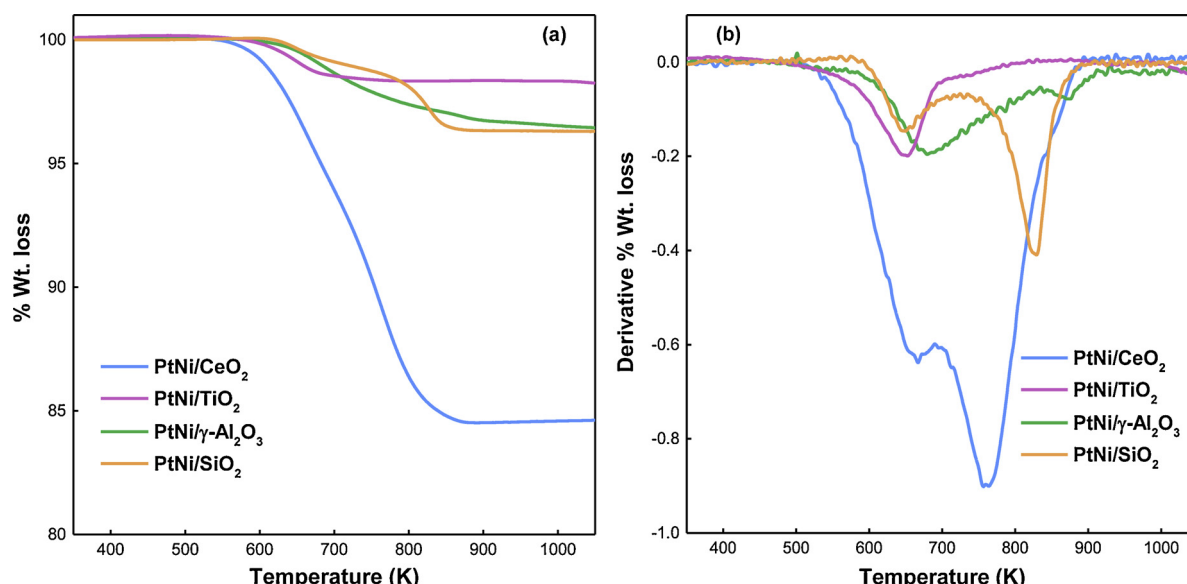


Fig. 5. (a) TG and (b) DTG plots of different spent Pt-Ni bimetallic catalysts. % Wt. loss and Derivative % Wt. loss represent the weight-normalized mass loss and the derivation of weight-normalized mass loss to ramping temperature, respectively. Note: for the sake of comparison, the TG plot of PtNi/CeO₂ was collected from the previous work [39].

Table 2

Deactivation extent and coke deposition on different PtNi supported catalysts.

Catalysts	Deactivation extent (%) ^a		I_G/I_D	Coke amount (% w.t. loss)	T_p^b (K)/ A_p^c (%)			
	CO_2	C_2H_6			Peak-1	Peak-2	Peak-3	Peak-4
PtNi/CeO ₂	8.99	16.15	0.72	15.5	664/51.2	767/46.3	846/2.5	-/0.00
PtNi/TiO ₂	29.99	33.77	0.75	1.7	642/87.1	747/5.5	940/0.9	1042/6.5
PtNi/ γ -Al ₂ O ₃	16.91	24.75	1.04	3.2	682/48.7	779/27.4	870/14.1	973/9.8
PtNi/SiO ₂	5.04	7.78	1.24	3.6	654/25.1	782/38.1	825/36.8	-/0.00

^a Deactivation extent is calculated based on reactants conversion between 147 and 672 min.^b Peak temperature of respective TPO-DTG peak, shown in the SI.^c Peak area (%) of respective TPO-DTG peak, shown in the SI.

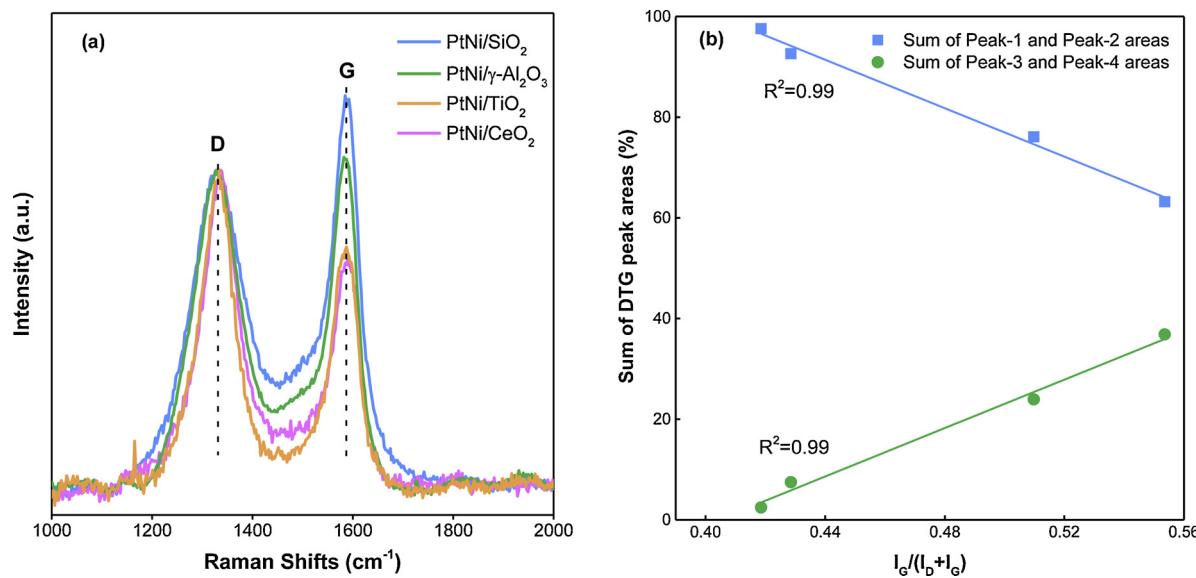
became noticeable, indicating the oxidation of Ni by the CO_2 -derived oxygen-containing species. However, the NiO peaks diminished after 20 min with the presence of a new stable peak at 6.66°. It should be noted that the weak peak centered at 6.06° should be assigned to Pt (111) by comparing the standard spectra in Fig. S6 in SI, indicating the presence of small amount of Pt fine particles. Given the peak positions of Pt(111) and Ni(111), it is reasonable to assign the peak at 6.66° to a Ni rich-PtNi intermetallic phase, consistent with the previous peak assignment [39]. The dynamic structural evolution during the initial reaction process (highlighted by the ellipse in Fig. 7(a) and Fig. S7, ~20 min) involved the formation of PtNi alloy structure. The PtNi alloy peak remained unchanged during the subsequent reaction and CO_2 treatment processes, suggesting the high stability of this structure. The PtNi/CeO₂ catalyst was then immediately reduced again at 873 K to check the temperature effect. It shows that the full-width-at-half-maximum (FWHM) of PtNi alloy slightly decreased, suggesting a slight increase in the metal particle size. However, Fig. S8(a) in SI suggested negligible effects of reduction temperature (723 K vs. 873 K) on the reactant conversions. As for PtNi/SiO₂ shown in Fig. 7(b), NiO peaks [(111): 5.66°, (200): 6.49°] were observed at room temperature and they became diminished with the increasing temperature under H_2 atmosphere. Additionally, two new peaks were observed at 6.34° and 6.66° from ~520 K, given the peak positions of Pt(111) (6.06°) and Ni (111) (6.80°), assigned to the Pt rich and Ni rich-PtNi intermetallic phases, respectively. The formed PtNi intermetallic or alloy structure maintained very stable regardless of being exposed to the reactant stream, CO_2 or H_2 at 873 K. The peaks of Pt, PtO and Ni were barely detected in the PtNi/SiO₂ catalyst. The *in situ* XRD analysis indicated

Table 3Quantification of CO_2 pulse results of the CeO₂, SiO₂, PtNi/CeO₂ and PtNi/SiO₂ samples.

Catalysts	CO ($\mu\text{mol/g}_{\text{cat}}$)/ Percentage (%)	Loss ($\mu\text{mol/g}_{\text{cat}}$)/ Percentage (%)	Consumed CO_2 ($\mu\text{mol/g}_{\text{cat}}$)
SiO ₂	0.0/-	0.0/-	0.0
CeO ₂	568.0/90.2	63.1/9.8	631.1
PtNi/SiO ₂	29.6/87.0	4.9/13.0	34.5
PtNi/CeO ₂	540.0/75.5	175.0/24.5	715.0

that PtNi alloy was the dominant metal phase on both the PtNi/SiO₂ and PtNi/CeO₂ catalysts even though the dynamic structural evolution started from much lower temperature (~520 K) on the former than that on the latter.

Fig. 8(a) and (b) showed the comparison of the DRIFT spectra of adsorbed CO at room temperature for the bimetallic Pt-Ni catalysts and the respective monometallic catalysts. As shown in Fig. 8(a), the vibrational frequency of adsorbed CO was used to identify whether the surface was terminated by Pt or Ni, and Pt-dominant Pt-Ni bimetallic surface was determined on the PtNi/CeO₂ catalyst in the previous work [39]. In Fig. 8(b), the peaks centered at 2061 cm^{-1} on Ni/SiO₂ was ascribed to the linear CO adsorption on Ni sites, while those at 1946 and 1873 cm^{-1} were attributed to the CO bonded to bridge Ni sites [63–65]. For Pt/SiO₂, it has been reported that peaks located in the regions of 2060–2086 cm^{-1} and 1840–1870 cm^{-1} are correlated with the linearly- and bridge-adsorbed CO on Pt sites, respectively [66,67]. In the present work, Pt/SiO₂ showed a dominant CO adsorption feature

**Fig. 6.** (a) Raman spectra of spent PtNi/SiO₂, PtNi/ γ -Al₂O₃, PtNi/TiO₂ and PtNi/CeO₂ catalysts; (b) Sum of DTG peak areas for the four spent PtNi bimetallic catalysts as a function of the ratio of $I_g/(I_d + I_g)$.

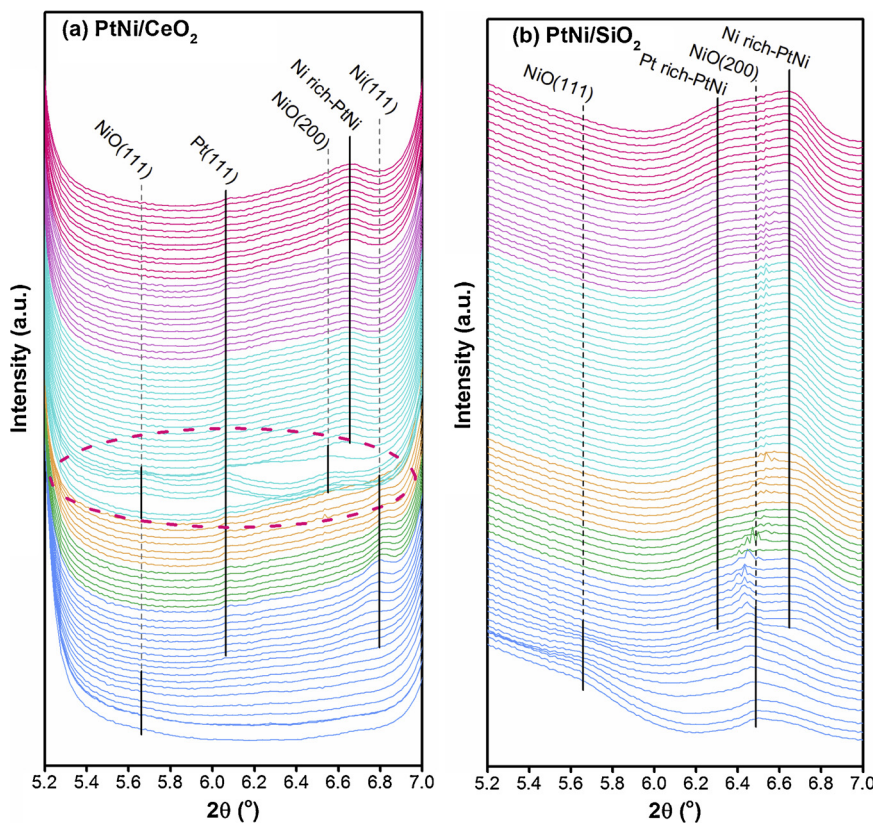


Fig. 7. Sequential *in situ* XRD spectra of PtNi/CeO₂ (a) and PtNi/SiO₂ (b) between 5.2° and 7.0° under different treatment conditions: heating from room temperature to 723 K (blue), reduction-1 (green), heating from 723 K to 873 K (orange), CO₂/C₂H₆/He = 1:1:2 (cyan), CO₂ only (purple), reduction-2 (red) (For interpretation of the references to colour in this figure legend, the reader is referred to the web version of this article).

at 2074 cm⁻¹ and was assigned to the linear adsorption on Pt sites; spectral weak peaks were observed within the region of bridge-bonded CO. Two noticeable peaks were observed at 2084 cm⁻¹ and 2074 cm⁻¹ on the PtNi/SiO₂ catalyst, which were similar to the spectral feature on Pt/SiO₂, while the characteristic features of CO adsorption on Ni were barely observed on PtNi/SiO₂. Thus, the comparison of the spectra on PtNi/SiO₂ with those on Pt/SiO₂ and Ni/SiO₂ also indicated a Pt-dominant Pt-Ni bimetallic surface termination on PtNi/SiO₂.

Given the above characterizations, PtNi/CeO₂ and PtNi/SiO₂ showed similar structural properties in terms of the CO uptake values,

the metal particle size distributions and the formation of PtNi intermetallic or alloy phase with the Pt-dominant surface termination. In addition, the coordination number (CN) ratio, CN_{Pt-Ni}/(CN_{Pt-Pt} + CN_{Pt-Ni}), based on the Pt L₃-edge EXAFS fitting data (**Table S3** in SI) suggested a similar alloying extent on PtNi/CeO₂ (70%) and PtNi/SiO₂ (63%) [68,69]. Recent DFT calculations reported that the Pt-dominant bimetallic (Pt-Ni) surface would weaken the surface O binding strength and facilitate the formation of *C₂H₆O intermediates, which contribute to the selective C-C bond cleavage of ethane to syngas [13,39].

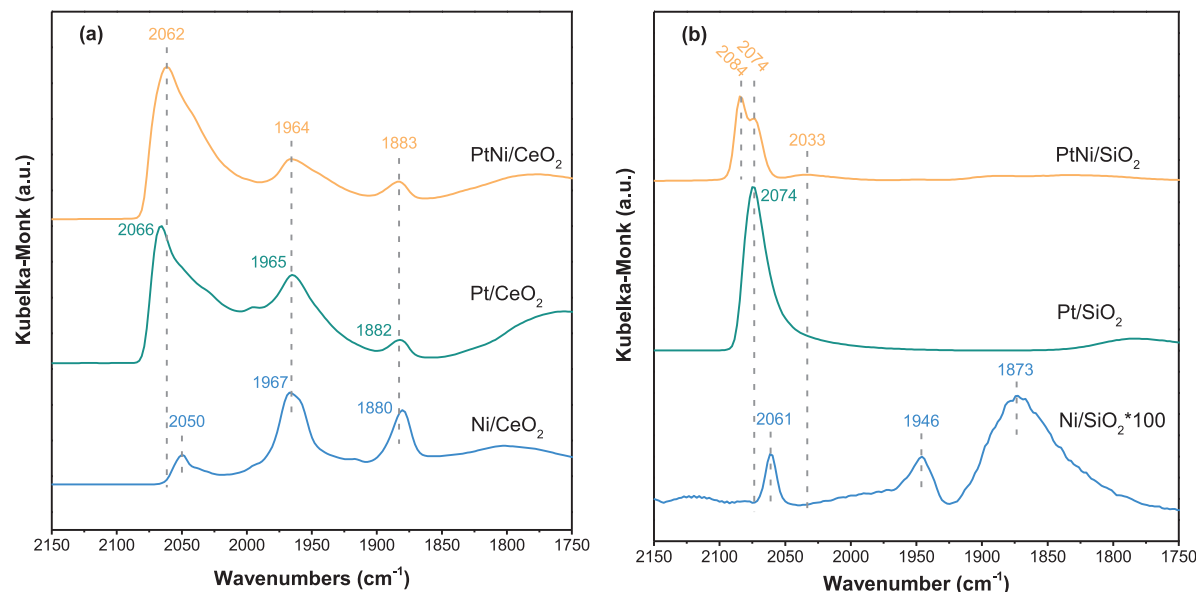


Fig. 8. DRIFT spectra of adsorbed CO at room temperature over reduced PtNi/CeO₂ (a) and PtNi/SiO₂ (b) as well as corresponding monometallic catalysts. Note: for the sake of comparison, the data for Fig. 8(a) were collected from the previous work [39].

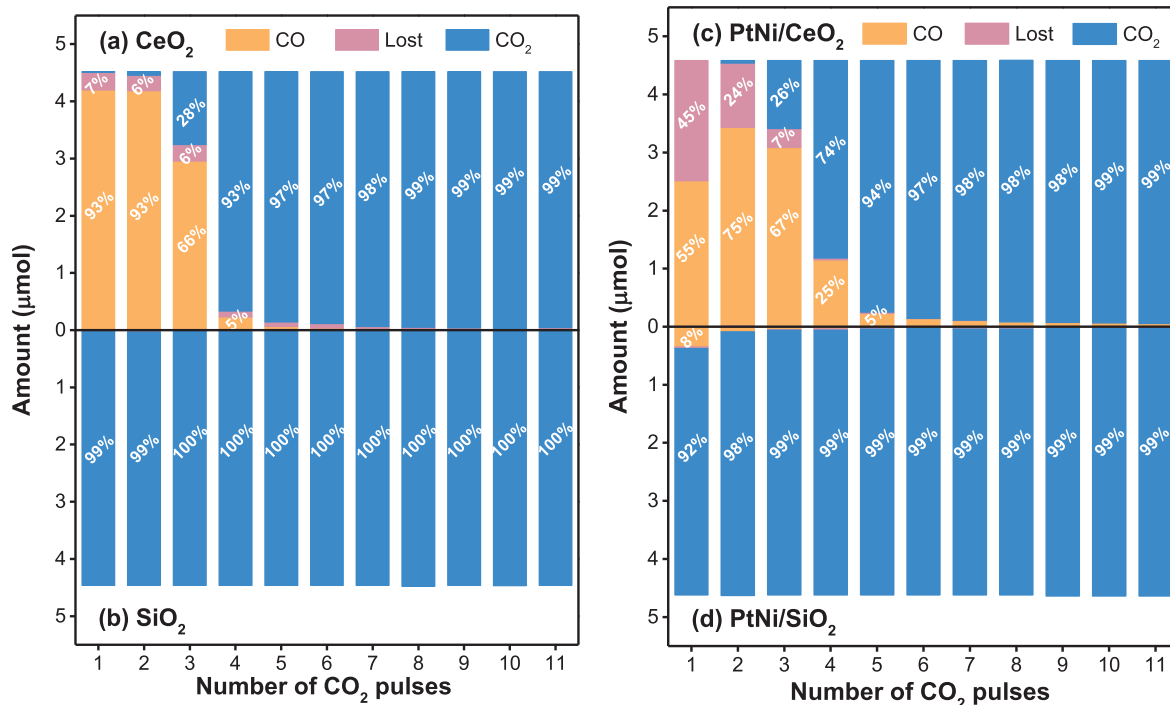


Fig. 9. CO₂ pulse experiments over the CeO₂ (a), SiO₂ (b), PtNi/CeO₂ (c) and PtNi/SiO₂ (d) catalysts. (T = 873 K, atmospheric pressure, 45 μmol for each pulse, CO₂/N₂ = 1:9, m = 20 mg).

3.3. Kinetics and mechanistic studies

3.3.1. Pulse reactor and flow reactor studies

To obtain a better understanding of the support effect on CO₂ activation, CO₂ pulse experiments were carried out for the pre-reduced catalysts (PtNi/CeO₂ and PtNi/SiO₂) as well as the pure supports (CeO₂, SiO₂). The CO₂ consumption profiles with product distributions along the consecutive pulses are shown in Fig. 9 (a)-(d). After the first CO₂ pulse, the reducible CeO₂ showed a significant CO₂ consumption, with the consumed CO₂ mainly being converted to CO (93%) and the remaining 7% producing surface species on CeO₂. Li et al. [70] carried out DRIFTS experiments to study the adsorption of CO₂ on CeO₂. They reported that CO₂ adsorption on CeO₂ resulted in the formation of carbonates and carboxylates. In the present work, similar DRIFT spectrum of CO₂ adsorption was observed (Fig. S9 in SI) at 723 K within the spectral range of 800 – 1650 cm⁻¹, confirming the formation of carbonates on CeO₂.

Rietveld refinement of the CeO₂ lattice parameter (Fig. S10(a) and (b) in SI) during the *in situ* XRD measurements revealed the transformation of Ce⁴⁺ to Ce³⁺ after H₂ reduction with the simultaneous formation of oxygen vacancies, which could be replenished via activating CO₂. Thus, the combined XRD and pulse reactor results suggested that CO₂ was effectively activated by the oxygen vacancies of the reducible CeO₂ mainly *via* the dissociative adsorption. In contrast, no CO₂ consumption was observed on the irreducible SiO₂, ruling out the possibility of adsorption and activation of CO₂ on SiO₂. After SiO₂ was loaded with Pt-Ni, CO₂ was slightly consumed (34.5 μmol/g_{cat}), however, it remained negligible compared with that on the pure CeO₂ (631.1 μmol/g_{cat}). This suggested that SiO₂ acted as a spectator and played no or negligible role in CO₂ activation. Thus, it is reasonable to propose that C₂H₆ and CO₂ were activated on the same metal site of PtNi/SiO₂.

After the deposition of Pt-Ni on CeO₂, the capacity of CO₂ activation was increased by 13.3%–715.0 μmol/g_{cat}, indicating that the co-existence of metal and reducible CeO₂ could further promote CO₂ activation. It should be noted that the percentage of CO formation decreased to 75.5%, while that of surface species increased to 24.5%.

Goguet et al. [71] investigated the surface species as CO₂ activated on Pt/CeO₂ during the RWGS reaction (498 K) by using DRIFTS-MS-SSITKA experiments. They found that the dominant species is carbonate, with carbonyl and formate also being produced. In the present work, the DRIFTS of CO₂ adsorption (see Fig. 13 in Section 3.3.2) also exhibited the similar surface species on PtNi/CeO₂.

To investigate the support effect on the C₂H₆ activation, C₂H₆ pulse experiments were carried out for PtNi/SiO₂ and PtNi/CeO₂ as well as the respective pure supports (SiO₂ and CeO₂). Prior to pulsing, catalysts were pretreated by H₂ or CO₂, named with suffix "-red" or "-oxi", respectively. Fig. 10(a)-(d) demonstrate the profiles of the accumulated amounts of consumed C₂H₆ and formed major carbon-containing species (CO, CO₂, CH₄, and adsorbed species) along consecutive C₂H₆ pulses. The pulse profiles of C₂H₄ were shown in Fig. S12 of SI, since the current work was focused on the support effects on the DRE reaction (C–C bond scission), instead of the ODEC reaction (C–H bond scission). The responses of pure supports (SiO₂ and CeO₂) to the C₂H₆ pulses were shown in Fig. S13(a) and (b) of SI.

Table 4 summarizes the quantification results of the total accumulated amount of each species with fourteen C₂H₆ pulses, after which the catalysts generally became saturated by the C₂H₆-derived species. Compared with the PtNi loaded catalysts, C₂H₆ was barely activated on both the irreducible SiO₂ (48.5 μmol/g_{cat}) and reducible CeO₂ (38.2 μmol/g_{cat}) supports. The PtNi/SiO₂-red catalyst showed a similar capacity of C₂H₆ activation with PtNi/SiO₂-oxi, with the former being slightly higher than the latter (*i.e.*, 1246.8 μmol/g_{cat} vs. 1046.9 μmol/g_{cat}), indicating the negligible effect of pretreatment with either H₂ or CO₂ on PtNi/SiO₂. Compared on PtNi/SiO₂-red, the amount of CO formed on PtNi/SiO₂-oxi was increased by 42.1 μmol/g_{cat}, consistent with the saturated amount (39.4 μmol/g_{cat}) of the adsorbed oxygen-containing species after the CO₂ pulses. This again suggested the negligible CO₂ activation on the metal sites if without any assistances, and consequently negligible contribution to C₂H₆ activation. Combined with the CO₂ pulse results, one can infer that, on the irreducible SiO₂-supported PtNi catalyst, CO₂ and C₂H₆ followed a mono-functional mechanism (*i.e.*, same metal active sites).

The pre-reduced PtNi/CeO₂ catalyst, PtNi/CeO₂-red, consumed a

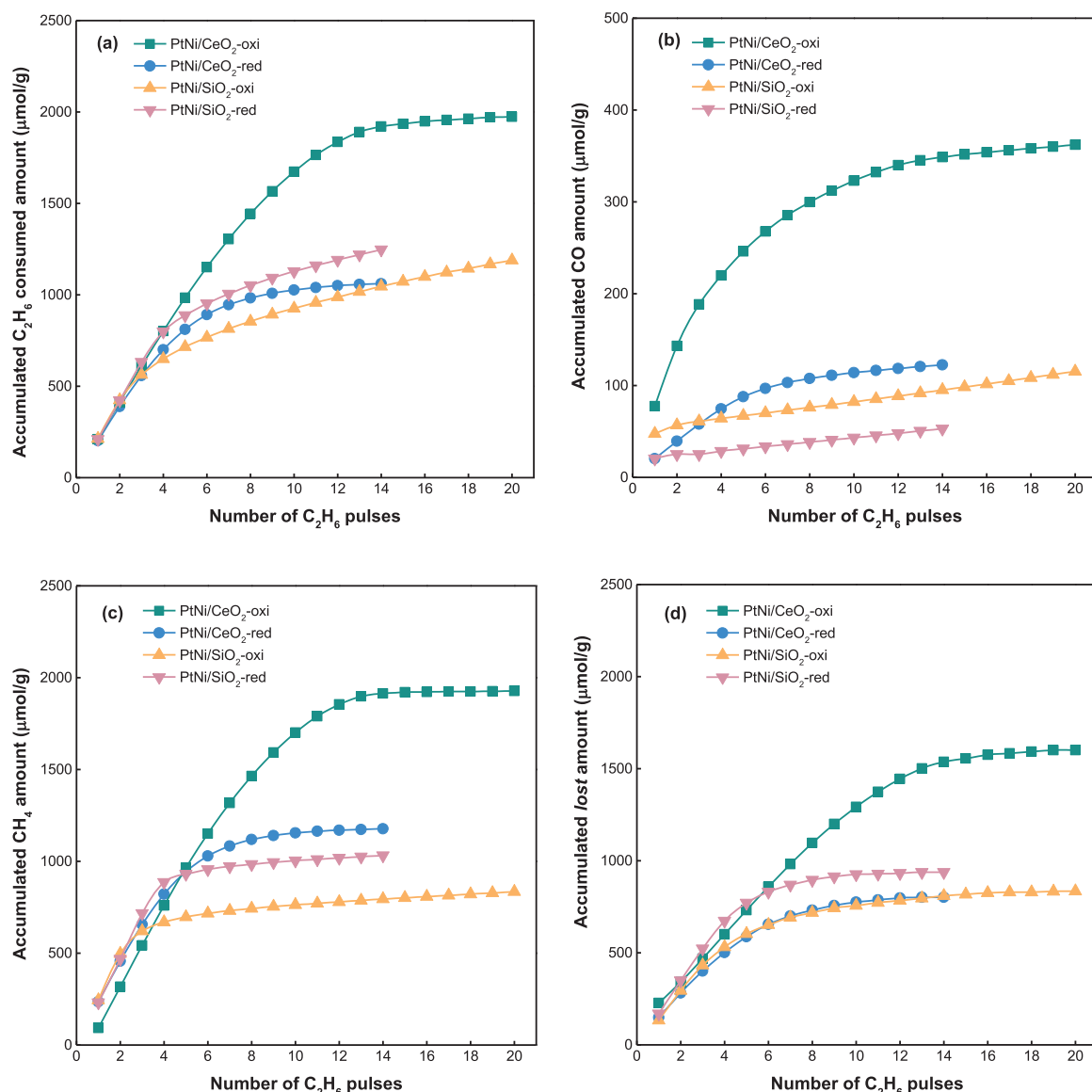


Fig. 10. Accumulated amounts of consumed C_2H_6 (a), formed CO (b), CH_4 (c) and adsorbed carbon-containing species (d) during a series of C_2H_6 pulses over the pre-reduced/oxidized PtNi/CeO_2 and PtNi/SiO_2 catalysts. ($T = 873\text{ K}$, atmospheric pressure, $45\text{ }\mu\text{mol}$ for each pulse, $\text{C}_2\text{H}_6/\text{N}_2 = 1:9$, $m = 20\text{ mg}$).

similar amount of C_2H_6 ($1061.3\text{ }\mu\text{mol/g}_{\text{cat}}$) with PtNi/SiO_2 -red and PtNi/SiO_2 -oxi. However, much more C_2H_6 was consumed ($1920.2\text{ }\mu\text{mol/g}_{\text{cat}}$) on PtNi/CeO_2 -oxi, revealing that the presence of the oxygen species from the CO_2 activation could significantly promote C_2H_6 activation. It should be noted that PtNi/CeO_2 -oxi showed a larger amount of lost surface carbon species ($1537.4\text{ }\mu\text{mol/g}_{\text{cat}}$) than $\text{PtNi}/$

SiO_2 (938.0 and $809.8\text{ }\mu\text{mol/g}_{\text{cat}}$), consistent with the comparison in the TGA analysis. Additionally, the DTG and Raman results indicated that the formed carbon species on the spent PtNi/CeO_2 catalyst were mainly active and disordered. This suggested that even though larger amounts of carbon species were formed on PtNi/CeO_2 than those on PtNi/SiO_2 , they mainly acted as the active intermediates for the reforming

Table 4

Quantification results after fourteen consecutive C_2H_6 pulses of the SiO_2 , CeO_2 , PtNi/CeO_2 and PtNi/SiO_2 catalysts.

Catalysts	Consumed $\text{C}_2\text{H}_6^{\text{a}}$	Consumed $\text{C}_2\text{H}_6^{\text{b}}$	CO	CO_2	CH_4	Loss ^c	C_2H_4
PtNi/ SiO_2 -red	1246.8	1011.3	53.0	0.0	1031.6	938.0	235.5
PtNi/ SiO_2 -oxi	1046.9	849.7	95.1	0.0	794.4	809.8	197.2
PtNi/ CeO_2 -red	1061.3	1050.2	122.6	0.0	1176.8	801.0	11.1
PtNi/ CeO_2 -oxi	1920.2	1912.3	348.8	23.7	1914.6	1537.4	7.9
SiO_2 -oxi	48.5	43.8	15.3	10.4	0.0	61.9	4.7
CeO_2 -oxi	38.2	21.0	4.2	2.7	0.6	34.4	17.2

Unit: $\mu\text{mol/g}_{\text{cat}}$.

^a represents the consumed amount of C_2H_6 taking into account of C_2H_4 .

^b represents the consumed amount of C_2H_6 without taking into account of C_2H_4 .

^c refers to the adsorbed carbon-containing species (C_1) on the catalyst, and its amount was quantified by carbon balance.

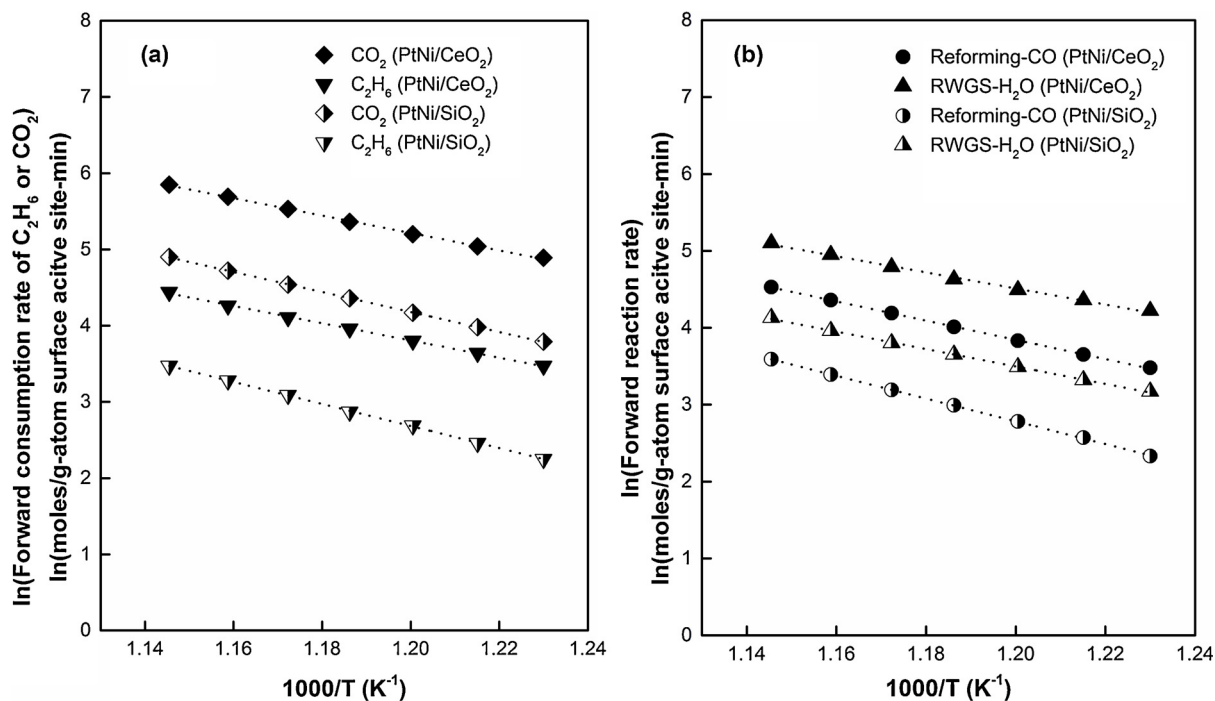


Fig. 11. Forward reaction rates as a function of reciprocal temperature on PtNi/CeO₂ [58] or PtNi/SiO₂ ($T = 813\text{--}873\text{ K}$, atmospheric pressure, $P_{\text{CO}_2} = 5\text{ mg}$, $m_{\text{PtNi/CeO}_2} = 5\text{ mg}$, $m_{\text{PtNi/SiO}_2} = 10\text{ mg}$).

reaction. In general, on the reducible CeO₂-supported PtNi catalyst, CO₂ and C₂H₆ should dominantly follow a bi-functional mechanism that CO₂ was mainly activated by the sites of CeO₂ or metal-support interface and the formed oxygen species decorated the metal sites or metal-oxide interface, on which C₂H₆ could be activated.

To investigate the support effect on the kinetics of DRE, kinetics measurements of activation barriers and partial pressure dependencies were carried out. Fig. 11 and Table 5 showed the activation barriers for the two catalysts, obtained via the forward reaction rates at temperatures between 813 and 873 K. The conversion of CO₂ showed a lower activation barrier than that of C₂H₆ on both catalysts, due to the concurrent RWGS reaction with lower activation barriers (87 and 94 kJ/mol over PtNi/CeO₂ and PtNi/SiO₂, respectively) than those of DRE (104 and 123 kJ/mol, respectively). PtNi/CeO₂ showed lower activation barriers than those of PtNi/SiO₂ for CO₂ (95 vs. 109 kJ/mol) and C₂H₆ (102 vs. 120 kJ/mol), consistent with the higher DRE activity of PtNi/CeO₂.

Fig. 12 shows the consumption rate of C₂H₆ to produce CO, i.e., the reforming rate, as a function of $P_{\text{C}_2\text{H}_6}$ from 6.25 kPa to 62.5 kPa at several constant CO₂ partial pressures. As shown in Fig. 12(a) and (b), the reforming rate followed different kinetics dependence on C₂H₆ over PtNi/SiO₂ and PtNi/CeO₂, especially at low partial pressures of CO₂ (e.g., 6.25 and 12.5 kPa). An inhibition effect, which was the typical feature of the competitive adsorption mechanism, clearly appeared over PtNi/SiO₂, suggesting that both CO₂ and C₂H₆ were activated on the same active site of PtNi/SiO₂, i.e., mono-functional (single-site) Langmuir-Hinshelwood (L-H) mechanism. In contrast, on PtNi/CeO₂, the reforming rate increased with the increase of $P_{\text{C}_2\text{H}_6}$ and then gradually

leveled off or slightly dropped, which was quite different from that on PtNi/SiO₂, implying that CO₂ and C₂H₆ most likely were activated on different active sites of PtNi/CeO₂, i.e., bi-functional (dual-site) Mars-Van Krevelen (MvK) mechanism.

3.3.2. *In situ* DRIFTS studies

Given the significant role of reducibility of oxide supports on CO₂ activation, more DRIFTS experiments were carried out to provide a mechanistic understanding of the activation of CO₂. Fig. 13(a) shows the DRIFT spectra on PtNi/CeO₂ and PtNi/SiO₂ during the flow of CO₂ or the mixture of CO₂ and H₂ at 773 K. For PtNi/SiO₂, the vibrational peak of linearly adsorbed CO was observed at 2042 cm⁻¹, suggesting a dissociative activation of CO₂ into carbonyl on the metal site, consistent with the pulse reactor analysis. The peaks in the region of 1300–1600 cm⁻¹ indicate the presence of formate species which likely formed from the interaction between formed CO and hydroxyl [70,72]. The involved hydroxyl should be produced during the reduction process. The co-feed of CO₂ and H₂ increased the intensity of carbonyl (2049 cm⁻¹) and formate species (1300–1600 cm⁻¹). It has been reported that the formed formate species could be further decomposed into CO and hydroxyl [73]. Combined with the pulse reactor studies, it is most likely that CO₂ activation on PtNi/SiO₂ proceeds with not only direct decomposition (CO₂+2*→CO*+O*) on metal sites but also H-assisted activation to formate species (CO₂+H*→formates) that could further decompose into linearly adsorbed CO on metal sites. The formed CO could desorb as gaseous CO (2180 and 2115 cm⁻¹).

In contrast, in addition to the presence of linearly adsorbed CO at 2038 cm⁻¹, carbonates species [71–73] were observed on PtNi/CeO₂ within the frequency range of 800–1600 cm⁻¹ during the CO₂ flow. This validated that CeO₂ could provide additional active sites for CO₂ activation, consistent with the results of CO₂ pulse analysis. After exposed to the mixture of CO₂ and H₂, PtNi/CeO₂ exhibited the presence of formate species (1300–1600 cm⁻¹) and new type of carbonate (800–1200 cm⁻¹). The DRIFTS experiments indicated at least four types of species related to CO₂ activation on PtNi/CeO₂: 1) CO₂+O*→carbonates (on oxide support); 2) CO₂+H*→formates (on metal or metal-oxide interface); 3) CO₂+2*→CO*+O* (on support or metal-oxide

Table 5
Activation barriers on the PtNi/CeO₂ and PtNi/SiO₂ catalysts.

Catalysts	Activation barriers (kJ/mol)			
	CO ₂	C ₂ H ₆	Reforming	RWGS
PtNi/CeO ₂ [58]	95	102	104	87
PtNi/SiO ₂	109	120	123	94

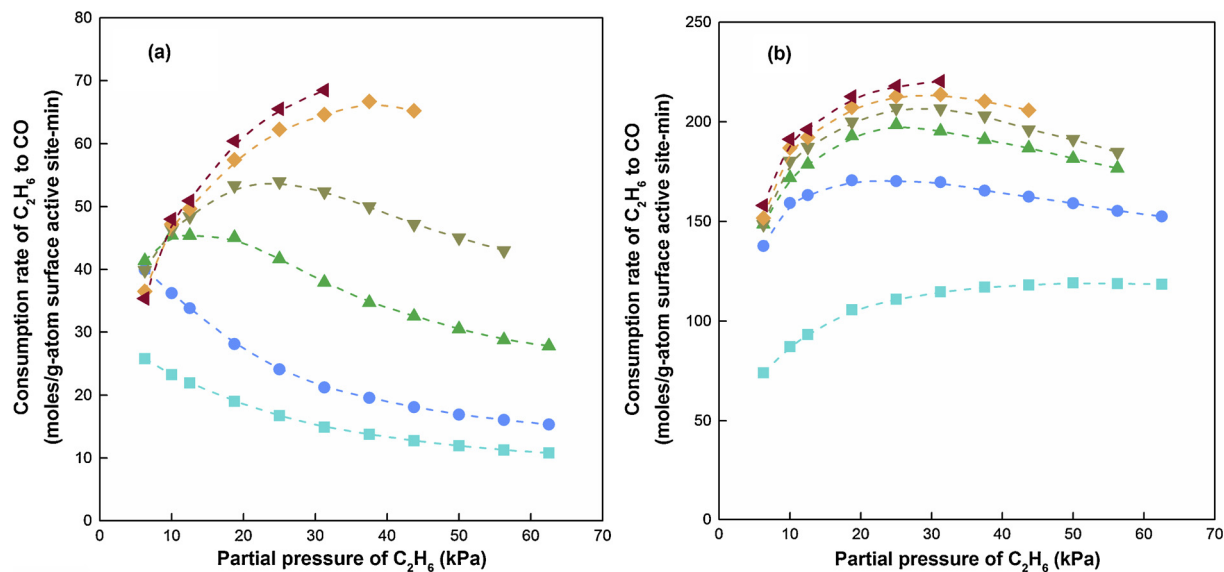


Fig. 12. Forward consumption rate of C_2H_6 to CO as a function of C_2H_6 partial pressure with 6.25 kPa (■), 12.5 kPa (●), 25 kPa (▲), 37.5 kPa (▼), 50 kPa (◆), 62.5 kPa (◀) of CO_2 on (a) PtNi/SiO₂ or (b) PtNi/CeO₂ (T = 873 K, 1 atm, $\text{CO}_2/\text{C}_2\text{H}_6/\text{Ar}$ = 10/10/60 ml/min, $m_{\text{PtNi/CeO}_2}$ = 5 mg, $m_{\text{PtNi/SiO}_2}$ = 10 mg).

interface); 4) $\text{CO}_2 + 2^* \rightarrow \text{CO}^* + \text{O}^*$ (on metal). The symbols of $\text{O}^\#$, * , and $*$ represent the lattice oxygen of CeO₂, oxygen vacancy of CeO_x, and active site of metal, respectively. Using the capacity of CO_2 activation (see Table 3) on PtNi/SiO₂ to represent the magnitude of step 4) on metal sites, step 3) should be the dominant pathway to produce the adsorbed oxygen species for ethane activation on PtNi/CeO₂. Therefore, combined with the C_2H_6 pulse reactor results, during the reforming reaction on PtNi/CeO₂, the oxygen species appeared to be primarily produced from step 3) on the oxide support or at the metal-oxide interface. These species likely react with C_2H_y^* (or H^*) formed from the ethane activation to promote the formation of ${}^*\text{C}_2\text{H}_y\text{O}$ [13] (or hydroxyl) species that finally produce CO or (OH or H₂O).

To investigate reaction pathways of the above proposed intermediates on PtNi/CeO₂, additional DRIFTS experiments were carried out. Initially, samples were reduced at 723 K and then exposed to the mixture of CO_2 and H₂ followed by the purging with only H₂ at 773 K. As shown in Fig. 13(b), vibrational peaks associated with carbonates, formates, carbonyl, and CO(g) were detected during the co-feed of CO_2

and H₂. However, after switching off CO₂, all the above peaks except the stable carbonates (800–1200 cm⁻¹) rapidly decreased, indicating that most of the surface intermediates could be further consumed by H^{*} or decomposed to complete the catalytic cycle by forming gaseous products (CO and H₂O). The majority of the carbonate species could be transformed into CO and H₂O via the formation of formate-type intermediates by H-assisted decomposition [73], leading to the formation of surface hydroxyl and gaseous CO.

Based on the refinements of *in situ* X-ray diffraction (XRD), reactor studies and DRIFTS analyses, dry reforming of ethane should follow a mono-functional L-H mechanism, with which CO_2 and ethane compete for the activation on the same metal active sites. In contrast, different active sites for reactants on PtNi/CeO₂ give rise to a bi-functional MvK redox mechanism which provides more active sites for ethane, reducing the competitive adsorption with CO_2 , than that on PtNi/SiO₂. In addition, the formed surface oxygen species on support or metal-support interface of PtNi/CeO₂ could facilitate the activation of ethane, consistent with the higher activity of PtNi/CeO₂ than that of PtNi/SiO₂.

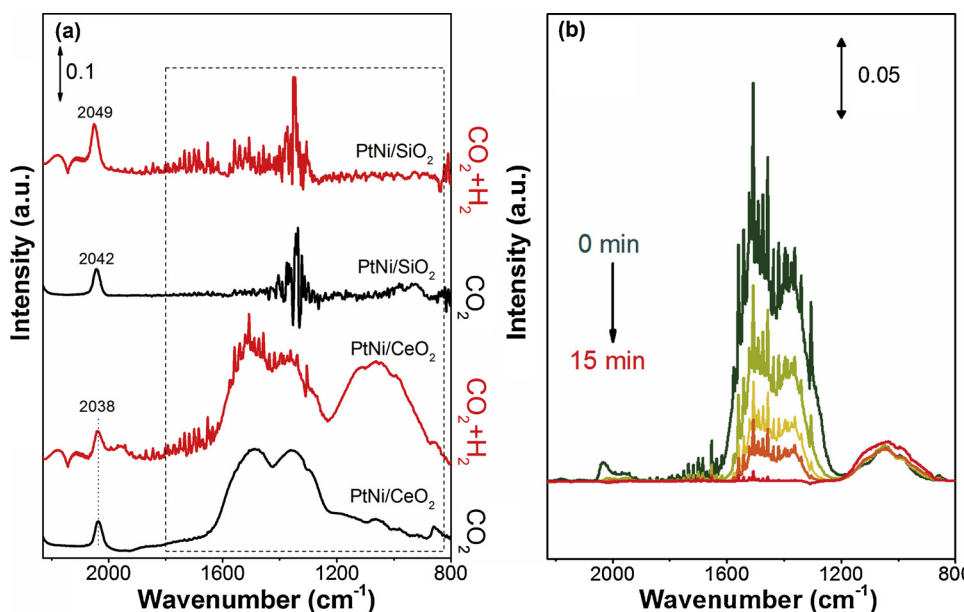


Fig. 13. (a) DRIFT spectra obtained on PtNi/SiO₂ and PtNi/CeO₂ under the flow of only CO_2 (black) and mixture of CO_2 and H₂ (red). Reaction conditions: T = 773 K, 1 atm, CO_2/He = 5/15 ml/min or $\text{CO}_2/\text{H}_2/\text{He}$ = 5/5/10 ml/min. (b) DRIFT spectra evolution with time on PtNi/CeO₂ after switching the flow from the mixture of CO_2 and H₂ to only H₂. Reaction conditions: T = 773 K, 1 atm, $\text{CO}_2/\text{H}_2/\text{He}$ = 5/5/10 ml/min for 30 min before the time of “0 min”, H_2/He = 5/15 ml/min (For interpretation of the references to colour in this figure legend, the reader is referred to the web version of this article).

4. Conclusions

Pt-Ni bimetallic catalysts have been supported on reducible oxides (CeO_2 and TiO_2) and irreducible oxides ($\gamma\text{-Al}_2\text{O}_3$ and SiO_2) and evaluated in terms of catalytic performance, structural properties, and reaction kinetics. Several conclusions can be drawn from the results:

- 1) The PtNi catalysts supported on reducible oxides (CeO_2 and TiO_2) were more active than those supported on irreducible oxides ($\gamma\text{-Al}_2\text{O}_3$ and SiO_2). PtNi/ CeO_2 showed promising reforming performance with the highest activity and CO yield among the four oxide supports.
- 2) Even though large amounts of carbon species were formed on PtNi/ CeO_2 , they were identified mainly as disordered/amorphous morphology, which acted as active intermediates and could be transferred from metals onto the support. PtNi/ TiO_2 was deactivated fast regardless of negligible carbon deposition, which was mainly due to the geometrical block of metal sites by TiO_x induced by SMSI. PtNi/ SiO_2 retained stable most likely benefiting from the strong metal–silica interaction and large surface area to accommodate carbon species. The deactivation of PtNi/ $\gamma\text{-Al}_2\text{O}_3$ mainly resulted from the metal agglomeration, Pt-Ni particles disintegration as well as the encapsulation by graphic carbon.
- 3) Dry reforming of ethane presented different kinetics behaviors on the irreducible SiO_2 and reducible CeO_2 supported catalysts: on PtNi/ SiO_2 , it followed a mono-functional Langmuir-Hinshelwood mechanism, subjected to the competitive adsorption of CO_2 and C_2H_6 on the same metal active sites; on PtNi/ CeO_2 , a bi-functional MvK redox mechanism dominated that CO_2 could be readily activated on the partially reduced CeO_2 or metal-CeO₂ interface, and the formed active oxygen species subsequently promoted ethane conversion.

Acknowledgments

We acknowledge support of this work under contract DE-AC02-98CH10886 with the U.S. Department of Energy (DOE) and supported by the Brookhaven National Laboratory Directed Research and Development (LDRD) Project No. 16-045. We also acknowledge the support by the National Natural Science Foundation of China (NSFC) under Grant No. 21673125 and 51876014. The *in situ* XRD measurements were performed at the 17 BM beamline at the Advanced Photon Source (APS).

Appendix A. Supplementary data

Supplementary material related to this article can be found, in the online version, at doi:<https://doi.org/10.1016/j.apcatb.2018.12.070>.

References

- [1] M.D. Porosoff, B. Yan, J.G. Chen, Energ. Environ. Sci. 9 (2016) 62–73.
- [2] J. Hansen, M. Sato, R. Ruedy, K. Lo, D.W. Lea, M. Medina-Elizade, Proc. Natl. Acad. Sci. 103 (2006) 14288–14293.
- [3] T.R. Knutson, R.E. Tuleya, J. Climate 17 (2004) 3477–3495.
- [4] N. Mimura, I. Takahara, M. Inaba, M. Okamoto, K. Murata, Catal. Commun. 3 (2002) 257–262.
- [5] M.D. Porosoff, M.N.Z. Myint, S. Kattel, Z. Xie, E. Gomez, P. Liu, J.G. Chen, Angew. Chem. Int. Ed. 54 (2015) 15501–15505.
- [6] M. Myint, B. Yan, J. Wan, S. Zhao, J.G. Chen, J. Catal. 343 (2016) 168–177.
- [7] D. Shekhawat, J.J. Spivey, D.A. Berry, Fuel Cells-Technologies for Fuel Processing, Elsevier, 2018.
- [8] D. Pakhare, J. Spivey, Chem. Soc. Rev. 43 (2014) 7813–7837.
- [9] Y.-g. Chen, K. Tomishige, K. Yokoyama, K. Fujimoto, Appl. Catal. A-Gen. 165 (1997) 335–347.
- [10] S.R. de Miguel, I.M.J. Vilella, S.P. Maina, D. San José-Alonso, M.C. Román-Martínez, M.J. Illán-Gómez, Appl. Catal. A-Gen. 435–436 (2012) 10–18.
- [11] M. García-Díez, I.S. Pieta, M.C. Herrera, M.A. Larrubia, L.J. Alemany, J. Catal. 270 (2010) 136–145.
- [12] M. García-Díez, I.S. Pieta, M.C. Herrera, M.A. Larrubia, L.J. Alemany, Appl. Catal. A-Gen. 377 (2010) 191–199.
- [13] S. Kattel, J.G. Chen, P. Liu, Catal. Sci. Technol. 8 (2018) 3748–3758.
- [14] G.L. Haller, D.E. Resasco, Adv. Catal. 36 (1989) 173–235.
- [15] S. Bernal, J. Calvino, M. Cauqui, J. Gatica, C.L. Cartes, J.P. Omil, J. Pintado, Catal. Today 77 (2003) 385–406.
- [16] M.C.J. Bradford, M. Albert Vannice, Catal. Today 50 (1999) 87–96.
- [17] A.P. Ferreira, D. Zanchet, J.C.S. Araújo, J.W.C. Liberatori, E.F. Souza-Aguiar, F.B. Noronha, J.M.C. Bueno, J. Catal. 263 (2009) 335–344.
- [18] M.V.M. Souza, D.A.G. Aranda, M. Schmal, J. Catal. 204 (2001) 498–511.
- [19] W.W. Lonergan, T. Wang, D.G. Vlachos, J.G. Chen, Appl. Catal. A-Gen. 408 (2011) 87–95.
- [20] D. Liu, X.Y. Quek, W.N.E. Cheo, R. Lau, A. Borgna, Y. Yang, J. Catal. 266 (2009) 380–390.
- [21] A. Tóth, G. Halasi, F. Solymosi, J. Catal. 330 (2015) 1–5.
- [22] A. Tóth, G. Halasi, T. Bánsági, F. Solymosi, J. Catal. 337 (2016) 57–64.
- [23] K. Nagaoka, K. Seshan, J.A. Lercher, K.-i. Aika, Catal. Lett. 70 (2000) 109–116.
- [24] S. Damyanova, B. Pawelec, K. Arshirova, M.M. Huerta, J. Fierro, Appl. Catal. B 89 (2009) 149–159.
- [25] H.C. Yao, Y.F.Y. Yao, J. Catal. 86 (1984) 254–265.
- [26] R. Wang, H. Xu, X. Liu, Q. Ge, W. Li, Appl. Catal. A-Gen. 305 (2006) 204–210.
- [27] T. Staudt, Y. Lykhach, N. Tsud, T. Skála, K.C. Prince, V. Matolín, J. Libuda, J. Catal. 275 (2010) 181–185.
- [28] P. Ferreira-Aparicio, I. Rodríguez-Ramos, J.A. Anderson, A. Guerrero-Ruiz, Appl. Catal. A-Gen. 202 (2000) 183–196.
- [29] B. Fu, J. Lu, P.C. Stair, G. Xiao, M.C. Kung, H.H. Kung, J. Catal. 297 (2013) 289–295.
- [30] M.D. Porosoff, M.N. Myint, S. Kattel, Z. Xie, E. Gomez, P. Liu, J.G. Chen, Angew. Chem. Int. Ed. 54 (2015) 15501–15505.
- [31] X. Lin, C.A. Hoel, W.M.H. Sachtleber, K.R. Poeppelmeier, E. Weitz, J. Catal. 265 (2009) 54–62.
- [32] F. Solymosi, A. Szoke, Appl. Catal. A-Gen. 166 (1998) 225–235.
- [33] C. Gillan, M. Fowles, S. French, S.D. Jackson, Ind. Eng. Chem. Res. 52 (2013) 13350–13356.
- [34] X. Huang, R. Reimert, Fuel 106 (2013) 380–387.
- [35] T. Wang, M.D. Porosoff, J.G. Chen, Catal. Today 233 (2014) 61–69.
- [36] W.W. Lonergan, D.G. Vlachos, J.G. Chen, J. Catal. 271 (2010) 239–250.
- [37] P.J. Chupas, K.W. Chapman, C. Kurtz, J.C. Hanson, P.L. Lee, C.P. Grey, J. Appl. Crystallogr. 41 (2008) 822–824.
- [38] W. Xu, R. Si, S.D. Senanayake, J. Llorca, H. Idriss, D. Stacchiola, J.C. Hanson, J.A. Rodriguez, J. Catal. 291 (2012) 117–126.
- [39] B. Yan, X. Yang, S. Yao, J. Wan, M. Myint, E. Gomez, Z. Xie, S. Kattel, W. Xu, J.G. Chen, ACS Catal. 6 (2016) 7283–7292.
- [40] A.P. Hammersley, S.O. Svensson, M. Hanfland, A.N. Fitch, D. Hausermann, High Pressure Res. 14 (1996) 235–248.
- [41] A.A.C. Larson, R.B. Von Dreele, Gsas. Report IAUR, (1994), pp. 86–748.
- [42] B.H. Toby, J. Appl. Crystallogr. 34 (2001) 210–213.
- [43] J.A. Dumesic, G.W. Huber, M. Boudart, Handbook of Heterogeneous Catalysis, Wiley-VCH Verlag GmbH & Co. KGaA, 2008.
- [44] T. Bligaard, R.M. Bullock, C.T. Campbell, J.G. Chen, B.C. Gates, R.J. Gorte, C.W. Jones, W.D. Jones, J.R. Kitchin, S.L. Scott, ACS Catal. 6 (2016) 2590–2602.
- [45] R.X. Valenzuela, G. Bueno, V. Cortés Corberán, Y. Xu, C. Chen, Catal. Today 61 (2000) 43–48.
- [46] R.X. Valenzuela, G. Bueno, V.C. Corberán, Y. Xu, C. Chen, Catal. Today 61 (2000) 43–48.
- [47] J. Anderson, Pergamon-Elsevier Science Ltd., The Boulevard, Langford Lane, Kidlington, Oxford OX5 1GB, England, 1963, pp. 147–148.
- [48] D.E. Mears, J. Catal. 20 (1971) 127–131.
- [49] H. Kubota, Y. Yamanaka, J. Chem. Eng. Jap. 2 (1969) 238–240.
- [50] H. Kubota, Y. Yamanaka, I.G.D. Lana, J. Chem. Eng. Jap. 2 (1969) 71–75.
- [51] V.W. Weekman Jr., R.L. Gorring, J. Catal. 4 (1965) 260–270.
- [52] P. Weisz, C. Prater, Adv. Catal. 6 (1954) 60390–60399.
- [53] J.J. Carberry, D. White, Ind. Eng. Chem. 61 (1969) 27–35.
- [54] S. Yagi, D. Kunii, AIChE J. 6 (1960) 97–104.
- [55] S. Yagi, D. Kunii, AIChE J. 3 (1957) 373–381.
- [56] D.E. Mears, Ind. Eng. Chem. Process Design Dev. 10 (1971) 541–547.
- [57] K. Jens, F. Stuft, F. Abild-Pedersen, T. Bligaard, Fundamental Concepts in Heterogeneous Catalysis, John Wiley & Sons, 2014.
- [58] Z. Xie, B. Yan, L. Zhang, J.G. Chen, Ind. Eng. Chem. Res. 56 (2017) 1360–1364.
- [59] J.E. Herrera, D.E. Resasco, J. Catal. 221 (2004) 354–364.
- [60] Y. Kaburagi, A. Yoshida, Y. Hishiyama, F. Kang (Ed.), Materials Science and Engineering of Carbon, Butterworth-Heinemann, 2016, pp. 125–152.
- [61] M.H. Brijaldo, H.A. Rojas, J.J. Martínez, F.B. Passos, J. Catal. 331 (2015) 63–75.
- [62] D. Liu, Y. Li, M. Kottwitz, B. Yan, S. Yao, A. Gamalski, D. Grolimund, O.V. Safonova, M. Nachtegaal, J.G. Chen, ACS Catal. 8 (2018) 4120–4131.
- [63] C. Mirodatos, H. Praliaud, M. Primet, J. Catal. 107 (1987) 275–287.
- [64] G. Martra, H. Swaan, C. Mirodatos, M. Kermarec, C. Louis, Studies in Surface Science and Catalysis, Elsevier, 1997, pp. 617–624.
- [65] D. Blackmond, E. Ko, J. Catal. 96 (1985) 210–221.
- [66] L. Deng, H. Miura, T. Shishido, S. Hosokawa, K. Teramura, T. Tanaka, Catal. Commun. 53 (2017) 6937–6940.
- [67] C. Vignatti, M. Avila, C. Apesteguía, T. Garetto, Int. J. Hydrogen Energ. 35 (2010) 7302–7312.
- [68] M.D. Porosoff, J.G. Chen, J. Catal. 301 (2013) 30–37.
- [69] S. Qi, B.A. Cheney, R. Zheng, W.W. Lonergan, W. Yu, J.G. Chen, Appl. Catal. A-Gen. 393 (2011) 44–49.
- [70] C. Li, Y. Sakata, T. Arai, K. Domen, K.-i. Maruya, T. Onishi, J. Chem. Soc., Faraday Trans. 1: Physical Chemistry in Condensed Phases 85 (1989) 929–943.
- [71] A. Goguet, F.C. Meunier, D. Tibiletti, J.P. Breen, R. Burch, J. Phys. Chem. B 108 (2004) 20240–20246.
- [72] N.M. Martin, P. Velin, M. Skoglundh, M. Bauer, P.-A. Carlsson, Catal. Sci. Technol. 7 (2017) 1086–1094.
- [73] L.F. Bobadilla, V. Garcilaso, M.A. Centeno, J.A. Odriozola, ChemSusChem 10 (2017) 1193–1201.